PHYSICAL REVIEW B **81**, 235416 (2010)

First-principles quantum transport theory of the enhanced wind force driving electromigration on Ag(111)

Kirk H. Bevan,[1,2,*] Hong Guo,[2] Ellen D. Williams,[3] and Zhenyu Zhang[1,4,5]
[1]*Materials Science and Technology Division, Oak Ridge National Laboratory, Oak Ridge, Tennessee 37831, USA*
[2]*Centre for the Physics of Materials and Department of Physics, McGill University, Montreal, Quebec, Canada H3A 2T8*
[3]*Department of Physics, University of Maryland at College Park, College Park, Maryland 20742-4111, USA*
[4]*Department of Physics and Astronomy, University of Tennessee, Knoxville, Tennessee 37996, USA*
[5]*ICQD, University of Science and Technology of China, Hefei, Anhui, China*
(Received 6 February 2010; revised manuscript received 8 April 2010; published 10 June 2010)

Herein we examine the *low-bias* electromigration wind force acting on quasi-one-dimensional nanoscale features within the Landauer-Büttiker conduction picture. Ordinarily the electromigration force is calculated under the approximation that the nonequilibrium carrier distribution in the vicinity of a defect is the same as that in the bulk. However, this approximation is rooted in the assumption that atomic scale defects scatter all incident electrons weakly (just as electrons weakly and diffusely scatter in the bulk). We examine this assumption by calculating the mode-resolved transmission against Ag(111) step edges and atomic wires using density-functional theory within the single-particle Green's function Landauer scattering picture. Furthermore we show that those modes that scatter strongly give rise to a nonequilibrium electrochemical potential drop across a defect and an increased wind force. The results quantitatively explain previously not understood experimental observations of an enhanced electron wind force against Ag(111) step edges [O. Bondarchuk *et al.*, Phys. Rev. Lett. **99**, 206801 (2007)]. In general, the results underscore the challenging nanoscale reliability problem posed by surface electromigration in nanostructures and the need for a nonequilibrium quantum transport description of the electron wind force.

DOI: 10.1103/PhysRevB.81.235416 PACS number(s): 71.15.−m, 73.22.−f, 73.40.−c, 73.63.−b

I. INTRODUCTION

As metal interconnects shrink toward and possibly beyond single nanometer dimensions,[1] increased surface roughness stands out as a critical nanoelectronics design challenge.[2,3] In addition to the added electrical resistance which arises from surface roughness scattering,[4] recent experimental observations[5–7] have suggested that nanoscale surface electromigration forces may be enhanced by up to an order of magnitude.[8,9] The electromigration wind force, usually characterized in terms of ballistic momentum transfer between flowing electrons and conductor atoms,[10] determines the structural reliability of a conductor. Any increase in the wind force accelerates the process of void formation and thereby reduces the lifetime of a conductor.[7] In nanoscale conductors void formation is even more problematic,[3] as rough surface features represent a sizable fraction of the conducting cross section and thereby provide ample opportunity for momentum transfer between conducting electrons and material atoms. Surface electromigration therefore represents a critical problem in the understanding and design of reliable nanoscale conductors.

The wind force acting on a nanoscale defect is determined by the scattered current.[10] The scattering current can be translated into a Hellmann-Feynman force by considering the nonequilibrium population of carriers in the vicinity of a defect.[11] Usually, the energetic distribution of carriers in the vicinity of a defect is assumed to be equivalent to that of the bulk material under bias.[11–14] The bulk nonequilibrium electron population under bias can be described by either the Boltzmann distribution[11] or Fermi distribution.[15] However, this picture only makes sense so long all incident carriers weakly scatter off a defect (just as they weakly and diffusely scatter in the bulk material).[16] Herein we test this approximation by calculating the transmission of each scattering electron mode. We find that though most modes scatter weakly, many scatter strongly off a defect site. Moreover, we argue that such "strongly" scattering electrons give rise to a nonequilibrium defect electrochemical potential drop[10,16,17] and result in an increased wind force estimate. The findings explain a previously not understood experimentally observed intensity in the electromigration force that is not captured by the bulk conduction picture.[5]

Motivated by reported studies[5,18] of an enhanced electromigration wind force on Ag(111) thin films, we adopt the Ag(111) surface as our model system for examining the *low-bias* electromigration wind force on nanoscale features. We consider the electromigration wind force acting on surface-situated atomic wires[19] and step edges[20,21] in both the bulk and local defect scattering regimes.[11–14,22–24] The wind force is calculated self-consistently using density-functional theory (DFT) within the single-particle Green's function Landauer-Büttiker electron-transport picture.[23–27] Bulk estimates of the wind force[11–14] are shown to fall below experimental values.[5] While revised estimates which consider the local nonequilibrium electron distribution[23] about a defect are found to agree well. In general, the results underscore the need for a nonequilibrium quantum transport description of the electron wind force.

The remainder of the paper is divided into three parts. We first outline the method applied, starting with a derivation of the electromigration wind force within the Landauer-Büttiker transport picture and followed by a reduction to the low-bias regime. Second, bulk and local defect numerical wind force estimates arrived at via self-consistent DFT single-particle Green's function[25–27] calculations are discussed in detail. Lastly, we summarize the results.

II. METHOD

In this section we outline our theoretical and simulation method in two parts. First, we express the wind force in terms of the low-bias Landauer-Büttiker ballistic conduction picture. Subsequently, we briefly outline the DFT single-particle Green's function transport method[25–27] and its application to low-bias numerical wind force calculations. The reader is encouraged to consult the single-particle Green's function transport[15,25–27] and electromigration wind force literature[11–14,28] which are often presented separately despite being closely related.[23,24]

A. Low-bias wind force

The low-bias electron wind force expression can be extracted from the two probe Landauer-Büttiker picture.[11,15,26–28] Within the DFT single-particle Green's function transport picture the electronic Hamiltonian force contribution to the ith atom at position $\mathbf{R}_i$ is given by[11,26–28]

$$\langle \mathbf{F}_e \rangle = -\sum_{k,s} [\langle \Psi_D^{(L)} | \nabla_{\mathbf{R}_i} \hat{H}_e | \Psi_D^{(L)} \rangle f_L(E) + \langle \Psi_D^{(R)} | \nabla_{\mathbf{R}_i} \hat{H}_e | \Psi_D^{(R)} \rangle f_R(E)], \tag{1}$$

where $\Psi_D^{(L,R)}$ are the left/right electron wave functions scattering into the device (D) from the contacts.[11,15,26] The above summation is performed over all momentum k and spin states s. Moreover, $f_{L,R}(E)=1/(1+e^{(E-\mu_{L,R})/k_BT})$ defines the Fermi occupancy of left/right scattering electrons. At zero bias when both reservoirs posses the same temperature T and electrochemical potential ($\mu_{eq}=\mu_L=\mu_R$), there is no net electron flux and the electron wind force is by definition *zero*. Under equilibrium conditions the attractive forces arising from the electronic Hamiltonian ($\hat{H}_e$) are in balance with repulsive nuclear forces.

When a bias is applied such that $\mu_L \neq \mu_R$, a net nonzero driving wind force $\mathbf{F}_w$ arises from the *elastic scattering* of current carrying electrons in addition to a direct force due to the applied field $\mathbf{F}_{\mathcal{E}}$.[10,29] The total nonequilibrium force $\mathbf{F}_e^{ne}$ can be determined by subtracting the zero-bias electronic-force contribution from the biased electronic-force contribution[11–14,28,30]

$$\begin{aligned}\langle \mathbf{F}_e^{ne} \rangle &= \langle \mathbf{F}_w \rangle + \langle \mathbf{F}_{\mathcal{E}} \rangle \\ &= \langle \mathbf{F}_e^{bias} \rangle - \langle \mathbf{F}_e^{eq} \rangle \\ &= -\sum_{k',s'} [\langle \Psi_D^{(L)} | \nabla_{\mathbf{R}_i} \hat{H}_e^{bias} | \Psi_D^{(L)} \rangle f_L(E) \\ &\quad + \langle \Psi_D^{(R)} | \nabla_{\mathbf{R}_i} \hat{H}_e^{bias} | \Psi_D^{(R)} \rangle f_R(E)] \\ &\quad + \sum_{k,s} [\langle \Psi_D^{(L)} | \nabla_{\mathbf{R}_i} \hat{H}_e^{eq} | \Psi_D^{(L)} \rangle f_{eq}(E) \\ &\quad + \langle \Psi_D^{(R)} | \nabla_{\mathbf{R}_i} \hat{H}_e^{eq} | \Psi_D^{(R)} \rangle f_{eq}(E)]. \end{aligned} \tag{2}$$

We define k' and s' to be the respective momentum and spin indices of electrons scattering into the device under bias. Note, that Eq. (2) also includes electric field $\mathcal{E}$ force contributions when electrostatic boundary conditions are applied at the contacts.[31]

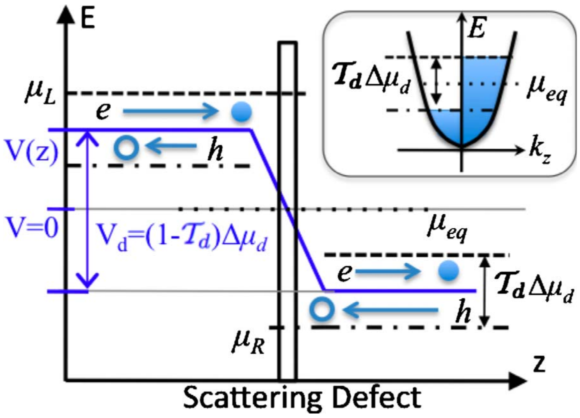

FIG. 1. (Color online) Scattering defect electrochemical potential splitting $\Delta\mu_d$ superimposed on its electrostatic potential drop V_d very close to the defect (much less than the electron mean-free path as compared to Fig. 5). We define $\mathcal{T}_d$ to be the low-bias transmission between the left μ_L and right μ_R electrochemical potentials (or quasi-Fermi levels), where the electrochemical potential splitting across the defect is given by $\Delta\mu_d=\mu_L-\mu_R$. The equilibrium electrochemical potential μ_{eq} sits midway between the nonequilibrium left μ_L and right μ_R electrochemical potentials. The inset shows the shifted momentum occupation for bulk conduction far from the scattering defect.

In the low-bias limit it is assumed[11–14,30] that the applied voltage is so small that the electronic Hamiltonian changes negligibly from its equilibrium state, such that $\hat{H}_e^{bias} \approx \hat{H}_e^{eq}$. The wind force contribution in Eq. (2) is thereby reduced to a sum over all states which lie within the conduction window[11–14,30]

$$\langle \mathbf{F}_w \rangle \approx -\sum_{k,s} \{ \langle \Psi_D^{(L)} | \nabla_{\mathbf{R}_i} \hat{H}_e^{eq} | \Psi_D^{(L)} \rangle [f_L(E) - f_{eq}(E)] + \langle \Psi_D^{(R)} | \nabla_{\mathbf{R}_i} \hat{H}_e^{eq} | \Psi_D^{(R)} \rangle [f_R(E) - f_{eq}(E)] \}. \tag{3}$$

The low-bias approximation is usually only valid when the *electrostatic* potential of the ith scattering atom at position $\mathbf{R}_i$ lies midway between the left μ_L and right μ_R *electrochemical* potentials.[16] This assumption holds for adatoms, step edges, and other atomic scale defects which form a resistivity dipole.[10,15–17] Within a resistivity dipole the left electrochemical potential is raised and the right electrochemical potential is lowered, such that the reference equilibrium electrochemical potential μ_{eq} lies midway between μ_L and μ_R.[15] The defect electrochemical splitting $\Delta\mu_d=\mu_L-\mu_R$ determines the wind force magnitude and is the unknown quantity that will be the focus of this paper.

The low-bias approximation may be understood through the single-mode scattering picture shown in Fig. 1. Under bias the left electrochemical potential is raised and the right electrochemical potential is lowered such that $\mu_L=\mu_{eq}$

$+\Delta\mu_d/2$ and $\mu_R=\mu_{eq}-\Delta\mu_d/2$,[16] where $\Delta\mu_d$ is the electrochemical potential drop across the defect. Given an electron transmission probability of $\mathcal{T}_d$, for a single conducting mode the resulting voltage drop across the defect is $V_d=\Delta\mu_d(1-\mathcal{T}_d)$.[15] For the purposes of this discussion we can view the current density in terms of left incident electron conduction $I_e=(2e^2/h)(\mathcal{T}_d\Delta\mu_d/2)$ and right incident hole conduction $I_h=(2e^2/h)(\mathcal{T}_d\Delta\mu_d/2)$, where the total current is given by $I=I_e+I_h$. The hole and electron currents relax far from the defect and balance to form the shifted momentum occupation as shown in the inset of Fig. 1. This is just another way of saying that charge neutrality is preserved in the bulk limit far from the scatterer, the number of states which gain momentum equals the number of states which lose momentum.

In the case of an atomic-sized defect, the width of the scatterer is so small that the electrostatic potential drop is not able to follow the electrochemical potential drop and a resistivity dipole develops.[10,15,17] Under bias the scattering atom is situated within a resistivity dipole at the reference electrostatic potential of $V(z)=0$, between the two electrochemical potentials (see Fig. 1). The dipole formed about the scatterer is due to an additional filling of states from μ_{eq} to μ_L (see Fig. 1) and an emptying of states from μ_R to μ_{eq} (see Fig. 1).[15,16] Within this picture the defect sees (as shown in Fig. 1), an additional electronic scattering force from left incident states between μ_{eq} and μ_L and a depletion (or absence) of scattering force from states between μ_R and μ_{eq}. From this simple description of wind force accumulation and depletion, due to respective left and right incident electrons, we arrive at the intuitive expression given by Eq. (3).

Lastly, within the low-bias response picture of metallic conduction the direct force in Eq. (2) is generally held to be much smaller than the wind force ($\mathbf{F}_{\mathcal{E}}\ll\mathbf{F}_w$) such that $\mathbf{F}_e^{ne}\approx\mathbf{F}_w$.[11,32] However, to first order the direct force can be estimated via the relation $\mathbf{F}_{\mathcal{E}}=Q_d\mathcal{E}_d$, where Q_d is the charge transferred between the bulk material and the defect and $\mathcal{E}_d$ is the defect-resistivity dipole field. The defect-resistivity dipole is assumed to drop within a screening length $\pm L_s$ such that $\mathcal{E}_d=V_d/2L_s=\Delta\mu_d(1-\mathcal{T}_d)/2L_s$. In this paper we primarily examine nonequilibrium contributions to $\mathbf{F}_w$ in the low-bias limit. A full self-consistent nonequilibrium electrostatic computation of $\mathbf{F}_{\mathcal{E}}$ via Eq. (2) is left to future work.[10]

B. Numerical wind force implementation

Our low-bias wind force simulation approach is outlined in this section. For further details on the self-consistent DFT single-particle Green's function transport method[25–27] the reader is referred to the literature.[25,33] For the sake of completeness we encourage the reader to consult comprehensive discussions on scattering in the single-particle Green's function transport formalism given in Refs. 24 and 25 (and all references therein).

Within the single-particle Green's function Landauer approach,[15,25–27] the low-bias [see Eq. (3)] charge-density deviation $\Delta\rho$ of a two probe system can be described in terms of left-incident and right-incident scattering electrons[26]

$$\begin{aligned}\Delta\rho &= \Delta\rho_L+\Delta\rho_R\\ &= \sum_{k,s}|\Psi_D^{(L)}|^2(f_L-f_{eq})+|\Psi_D^{(R)}|^2(f_R-f_{eq})\\ &= \int_{-\infty}^{+\infty}\{G\Gamma_LG^\dagger[f_L-f_{eq}]+G\Gamma_RG^\dagger[f_R-f_{eq}]\}\frac{dE}{\pi},\end{aligned} \tag{4}$$

where we assume spin degeneracy in the energy integral. The quantities $\Delta\rho_L$ and $\Delta\rho_R$ describe the left and right nonequilibrium scattering electron densities.[15] Furthermore, the retarded Green's function of the device scattering region is numerically obtained via

$$G(E)=[(E+i\eta)S-H_e-\Sigma_L(E)-\Sigma_R(E)]^{-1}, \tag{5}$$

where η is a small positive infinitesimal constant and S is the overlap matrix between atomic basis functions.[25,33] The quantities $\Sigma_{L,R}$ are the self-energies of the left/right contacts, and $\Gamma_{L,R}=i(\Sigma_{L,R}-\Sigma_{L,R}^\dagger)$ describes the coupling between the device scattering region and the semi-infinite device leads.[15]

The DFT time-independent electronic Hamiltonian within Eq. (5) can be expressed as[34,35]

$$\hat{H}_e=-\frac{1}{2}\nabla^2+\hat{V}_{ps}^{nl}+V^{NA}+\delta V^H+V^{XC}, \tag{6}$$

where $\hat{V}_{ps}^{nl}$ is the nonlocal pseudopotential term, V^{NA} is the sum of all screened neutral atom potentials, δV^H is self-consistent Hartree term, and V^{XC} is the exchange-correlation term. We can further collapse all local terms into the reduced expression $V^l(\mathbf{r})=V^{NA}+\delta V^H+V^{XC}$. By combining Eqs. (4) and (6) with Eq. (3) to give

$$\langle\mathbf{F}_w\rangle=-\left[\sum_{jk}\Delta\rho_{jk}\langle\phi_j|\nabla_{\mathbf{R}_i}\hat{V}_{ps}^{nl}|\phi_k\rangle+\int\Delta\rho(\mathbf{r})\nabla_{\mathbf{R}_i}V^l(\mathbf{r})d\mathbf{r}\right]. \tag{7}$$

we arrive at a DFT single-particle Green's function[25–27] low-bias expression for the ballistic wind force in the presence of a stationary (or floating) basis.[28] The real-space charge density is obtained from the density matrix elements of the chosen local atomic orbital basis ϕ_i via $\Delta\rho(\mathbf{r})=\Sigma_{ij}\Delta\rho_{ij}\phi_i(\mathbf{r})\phi_j^*(\mathbf{r})$.

III. WIND FORCE ESTIMATES

With a model approach in hand, we now proceed to examine the Ag(111) surface electromigration wind force.[8] Throughout the analysis our results are benchmarked against experimental measurements of the Ag(111) surface electromigration wind force.[5,18] In Sec. III A the Ag(111) surface scattering geometries are outlined in detail, as are the DFT single-particle Green's function calculation model details.[25–27] Subsequently, Sec. III B presents a comprehensive discussion of the calculated bulk wind force with respect to the chosen geometries. Lastly, in Sec. III C we address the weak scattering assumption applied in the bulk wind force picture and argue that local resistivity dipole[16] scattering perturbations to the bulk electrochemical splitting should be considered in wind force estimates.

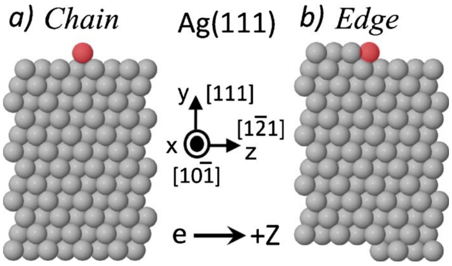

FIG. 2. (Color online) Ag(111) 12-layer surface scattering device geometries: (a) One-dimensional atomic chain and (b) scattering step edge. Semi-infinite 12-layer left and right contacts are included to calculate electron scattering and transport characteristics (Ref. 33). In each case the device region is repeated infinitely along the transverse x vector pointing out of the page to form a two-dimensional slab. In each geometry the scattering atom, for which the wind force is calculated, is highlighted in red (see Secs. II B and III).

A. Scattering geometries and model details

The theoretically investigated Ag(111) surfaces consist of 12 atomic layers periodically repeated to form slabs with [111] (Ref. 5) crystal orientations as shown in Fig. 2. Note that the DFT single-particle Green's function scattering[25–27] device regions are coupled to semi-infinite leads accounted for by self-energy terms in the device Green's function[33] (see Sec. II B). The left and right two probe leads are constructed of clean Ag(111) 12-layer slabs. The studied geometries were not relaxed and therefore retain the bulk bonding Ag lattice constant of 4.09 Å.[36] In this regard, it is important to note that the experimental Ag(111) thin films[5,18] consist of step edges and kinks randomly oriented along various facets transverse to the [111] direction. A detailed wind force study along the various relaxed facets is left to future work.

To compute the electronic-structure properties of the slabs displayed in Fig. 2, the local density approximation was employed in conjunction with a double-ζ-polarized basis set and Ag scalar relativistic Troullier-Martins[37] pseudopotentials. The basis set was confined at 0.0025 Ry (Ref. 35) and provided a bulk work function of 4.29 eV in agreement with plane-wave calculations.[38] A 12.5 Å vacuum buffer region was placed between the top and the bottom of each slab. The real-space grid sampling, as shown in Fig. 3, was set at four points per Bohr. In each calculation a convergence criteria of 10^{-5} was applied to both the Hamiltonian and density matrices. Furthermore, each system was sampled at $40 k_x$ points to capture transverse Blöch periodicity perpendicular to the z direction of transport.

TABLE I. Electrochemical splitting $\Delta\mu$ required to drive experimental current densities (Ref. 5) J through Ag(111) 12-layer slab geometries and bulk Ag(111) at the temperatures T. The bias window averaged transmission per unit area $\mathcal{T}/A$ is given as a metric for the scattering strength (units of conductance quantum G_0 per nm^2). The leads attached to each scattering region are clean and perfectly crystalline.

System	J (A/cm^2)	T (K)	$\Delta\mu$ (eV)	$\mathcal{T}/A$ (G_0/nm^2)
Ag(111)	8×10^5	350	0.934×10^{-5}	11.0444
Clean	2×10^5	370	0.234×10^{-5}	11.0443
Ag(111)	8×10^5	350	0.996×10^{-5}	10.3539
Chain	2×10^5	370	0.249×10^{-5}	10.3546
Ag(111)	8×10^5	350	1.024×10^{-5}	10.0720
Step	2×10^5	370	0.256×10^{-5}	10.0705
Ag(111)	8×10^5	350	0.916×10^{-5}	11.2655
Bulk	2×10^5	370	0.229×10^{-5}	11.2662

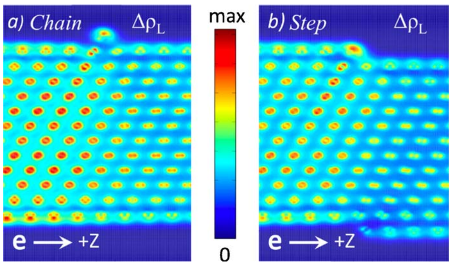

FIG. 3. (Color online) Unitless real-space plots of the left-scattering electron density $\Delta\rho_L$ at a driving current density of 8 $\times10^{-5}$ A/cm^2 as given by Eq. (4).

Electrochemical biases $\Delta\mu$ required to drive the reported experimental current densities[5] J are provided in Table I. The assumed current densities of 8×10^5 and 2×10^5 A/cm^2 include constriction due to 50% pitting of the experimental[5,18] thin films. The bias calculations were repeated for the geometries show in Fig. 2 as well as clean 12-layer Ag(111) and bulk Ag(111). Experimental temperatures are included through the Fermi occupation function [see Eq. (1)]. From Table I it is apparent that the clean Ag(111) 12-layer slab current capacity is nearly equivalent to that of bulk Ag(111). Moreover, the chain and step edge scatters only slightly perturb the clean slab bias window averaged transmission per unit area ($\mathcal{T}/A$) by about 10%. Therefore we conclude that the assumed 12-layer scattering geometry[38] reasonably approximates the bulk like 100-nm-thick experimental[5,18] thin films. Given the slight transmission difference between bulk Ag(111) and the 12-layer geometries, we assume the bulk $\Delta\mu_b$ electrochemical biases given in the fourth column of Table I in all subsequent calculations. For details regarding DFT single-particle Green's function current-density calculations we refer the reader to the literature.[25–27,33]

B. Bulk wind force

In this section we examine the wind force under the simplest approximation, namely, that the defect electrochemical splitting is well approximated by the bulk electrochemical splitting $\Delta\mu_d \approx \Delta\mu_b$. This is equivalent to assuming that the carrier distribution in the vicinity of a defect is well described by the bulk conduction picture with a shifted Fermi sphere (see insert in Fig. 1).[15] In Sec. III C we discuss this weak scattering approximation in detail and investigate whether it is justified.

In order to conceptualize the electron wind force it is helpful to examine the scattering electron density. Real-space

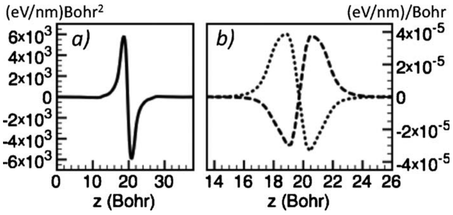

FIG. 4. Ag(111) atomic chain surface defect local potential contribution V^l to the z-direction bulk wind force at a driving current of 8×10^{-5} A/cm^2 [see Figs. 2(a) and 3(a)]. Figure 4(a) displays the local potential derivative as the integral $\int\partial V^l/\partial\mathbf{Z}_i dxdy$. Figure 4(b) displays the force integrals $F^l_{w_b,L}(z)=-\int\Delta\rho_L\partial V^l/\partial\mathbf{Z}_i dxdy$ (dashed) and $F^l_{w_b,R}(z)=-\int\Delta\rho_R\partial V^l/\partial\mathbf{Z}_i dxdy$ (dotted).

plots of the left incident scattering electron density $\Delta\rho_L$ are provided in Fig. 3 (see Sec. II), where incident electron[39] reflection is evident in the increased magnitude of $\Delta\rho_L$ to the left of both defects. The reflected electron density represents *elastic momentum transfer* between conducting electrons the atomic lattice. Current carrying electrons travel in the $+z$ direction and those that reflect transfer momentum to the defect; momentum transferred over time due to the continuous flow of electrons gives rise to a net wind force.

The bulk wind force due to conducting electrons can be further visualized via the local force contribution $F^l_{w_b}=-\int\Delta\rho\partial V^l/\partial\mathbf{Z}_i d\mathbf{r}$ [see Eq. (7)]. We emphasize that the total wind force also includes a nonlocal contribution due to the Kleinman-Bylander pseudopotential method applied.[35] The Ag(111) 12-layer atomic chain local potential derivative $\partial V^l/\partial\mathbf{Z}_i$ is plotted in Fig. 4(a), where the x and y dimensions are integrated over to provide a simplified plot in the z direction [see also Fig. 2(a)]. From Fig. 4(a) we see that $\partial V^l/\partial\mathbf{Z}_i$ is *antisymmetric* about the atomic origin. Furthermore, note that the scattering electron $\Delta\rho_{L,R}$ density is *asymmetric within* the surface situated atomic chain [see Fig. 3(a)]. Since $\Delta\rho_L$ provides an asymmetric accumulation and $\Delta\rho_R$ provides an asymmetric depletion of scattering states within the scattering atom, the force integrals $F^l_{w_b,L}=-\int\Delta\rho_L\partial V^l/\partial\mathbf{Z}_i d\mathbf{r}$ and $F^l_{w_b,R}=-\int\Delta\rho_R\partial V^l/\partial\mathbf{Z}_i d\mathbf{r}$ are both net positive as shown in Fig. 4(b). Under bias the left-incident states transfer more momentum (via accumulation) to the defect and the right-incident states transfer less momentum to the defect (via depletion). Both mechanisms act to provide a net wind force in the $+z$ direction of electron transport (see also Fig. 1 and the supporting discussion in Sec. II).

The calculated values of the bulk wind force F_{w_b} are displayed in Table II. To determine the wind force via Eq. (7), the highlighted atoms in Fig. 2 were displaced self-consistently ±0.001 Å in the y direction and transport z direction. The y-direction wind force arises from waveguide like[40] current carrying states with both k_y and k_z momentum, where k_y momentum is quantized in the plane of the slab.[41] The x-direction wind force is zero, due to equal and opposite scattering momentum contributions from $\pm k_x$ transverse states in the plane of the slab. The y-direction wind force on the chain highlighted in Fig. 2(a) is essentially zero due to equal and opposite contributions from $\Delta\rho_L$ and $\Delta\rho_R$ incident electrons. However in the vicinity of the step edge defect highlighted in Fig. 2(b), left-incident electrons $\Delta\rho_L$ scatter with greater intensity than right-incident electrons $\Delta\rho_R$ [see also Fig. 3(b)] giving rise to a nonzero y-direction wind force term. The y-direction wind force on the step edge highlighted in Fig. 2(b) accounts for 40% of F_{w_b} in Table II (at both current densities). The unitless effective charge values in Table II were obtained by dividing the calculated wind force by the bulk electric field such that $Z^*_{w_b}=F_{w_b}/\mathcal{E}_b$ (both in units of eV/nm). The bulk electric field is obtained through Ohm's law $\mathcal{E}_b=J_b/\sigma$, where we assume the bulk conductivity value $\sigma=(2.2\times10^{-6}\ \Omega\ \text{cm})^{-1}$ at 370 K.[5]

As is evident in Table II, the calculated values of the bulk wind force F_{w_b} and effective charge $Z^*_{w_b}$ lie below reported experimental values.[5] Yet, the results do indicate an increase in the step-edge effective charge estimate at $Z^*_{w_b}=-73$ on Ag(111) compared to an earlier study of the wind force against Al(100) step edges where the effective charge was found to be $Z^*_{w_b}=-43$.[9] In the experimental system electromigration occurs primarily along island and step edges[5,18] hence the true wind force value is likely to lie somewhere between that of the chain geometry [Fig. 2(a)] and the step geometry [Fig. 2(b)]. Taking the average calculated value of $Z^*_{w_b}\approx-65$, we arrive at a bulk estimate outside of the experimental error margin where on average $Z^*_{exp}\approx-186\pm93$. This shortfall is puzzling[5] and leads us to test the validity of the simple assumption $\Delta\mu_d\approx\Delta\mu_b$ in the next section (Sec. III C).[42,43]

Lastly, in the weak scattering regime the local-defect electric field equals the bulk electric field $\mathcal{E}_d=\mathcal{E}_b$. Therefore, the

TABLE II. Calculated Ag(111) wind force against the chain and step-edge atoms highlighted in Fig. 2 for the reported experimental current densities (Ref. 5). Bulk wind-force F_{w_b} and effective-charge $Z^*_{w_b}$ values are computed assuming weak scattering $\Delta\mu_d\approx\Delta\mu_b$ in the vicinity of each defect (see Sec. III B). The defect wind-force F_{w_d} and defect-effective-charge $Z^*_{w_d}$ values are estimated via the first-order defect-scattering model discussed in Sec. III C. The bulk and defect direct electric field forces are given in terms of the effective charges $Z^*_{\mathcal{E}_b}$ and $Z^*_{\mathcal{E}_d}$. The experimental wind-force $F_{w_{exp}}$ and effective-charge Z^*_{exp} values are taken from Ref. 5.

System	J (A/cm^2)	T (K)	$\Delta\mu_b$ (eV)	F_{w_b} (eV/nm)	$Z^*_{\mathcal{E}_b}$	$Z^*_{w_b}$	F_{w_d} (eV/nm)	$Z^*_{\mathcal{E}_d}$	$Z^*_{w_d}$	$F_{w_{exp}}$ (eV/nm)	Z^*_{exp}
Ag(111)	8×10^5	350	0.92×10^{-5}	1.02×10^{-5}	1.5×10^{-2}	-58	1.87×10^{-5}	2.6	-106		
Chain	2×10^5	370	0.23×10^{-5}	0.26×10^{-5}	1.5×10^{-2}	-58	0.47×10^{-5}	2.6	-106		
Ag(111)	8×10^5	350	0.92×10^{-5}	1.28×10^{-5}	9.5×10^{-3}	-73	2.30×10^{-5}	1.6	-131	$(2.70\pm1.35)\times10^{-5}$	-153 ± 76
Step	2×10^5	370	0.23×10^{-5}	0.32×10^{-5}	9.5×10^{-3}	-73	0.57×10^{-5}	1.6	-131	$(0.97\pm0.49)\times10^{-5}$	-220 ± 110

applied field imparts a direct force of $F_{\mathcal{E}_b}=Q_d\mathcal{E}_b$ (as discussed in Sec. II). The defect charge Q_d is quantified as the amount of charge transferred to or from the neutral bulk slab. The chain and step-edge defects highlighted in Fig. 2 both transfer a fractional number of electrons to the 12-layer Ag(111) slab, where the Q_d values were computed to be $1.5\times10^{-2}e$ and $9.5\times10^{-3}e$, respectively (note $e=1.6\times10^{-19}$ C). These defect charge values are directly comparable to the bulk wind force effective charge values in Table II since the bulk direct effective charge is given by $Z^*_{\mathcal{E}_b}=F_{\mathcal{E}_b}/\mathcal{E}_b=Q_d$. Evidently, the bulk direct force lies far below the bulk wind force $Z^*_{w_b}\approx-65$ and can be largely ignored.

C. Defect wind force

In this section we analyze the scattering strength of Ag(111) chain and step-edge surface defects. First, it is shown that such defects do not generally reside in the weak scattering limit where the assumption $\Delta\mu_d\approx\Delta\mu_b$ may be applied. Second, we go beyond the weak scattering picture to provide a first-order model estimate of the nonequilibrium local electrochemical splitting $\Delta\mu_d$ and wind force F_{w_d}. The nonequilibrium corrections yield an improved estimate of the wind force with respect to experimental measurements.[5]

1. Bulk and defect scattering

Diffuse phonon scattering dominates the low-bias resistivity of Ag(111) thin films at temperatures in excess of 275 K.[5,44] Diffuse scattering[17] can be approximated in terms of an average local bulk resistance[45] $R_b=(1-\mathcal{T}_b)h/\mathcal{T}_b2e^2$ per conducting mode contributed at each atomic lattice site (spin degeneracy is assumed). The parameter $\mathcal{T}_b$ defines the onsite scattering transmission per mode $(0\leq\mathcal{T}_b\leq1)$. This model approach is sketched in Fig. 5. In the diffuse scattering regime the electrochemical potential follows the electrostatic potential and both drop linearly across the conductor[17] (highlighted in red). By summing sum over the average resistance contributed at each lattice site by each mode (M) we arrive at the conductivity expression[15]

$$\sigma=\left(\nu_b\frac{1-\mathcal{T}_b}{\mathcal{T}_b}\frac{hA}{2Me^2}\right)^{-1}, \tag{8}$$

where ν_b denotes the number of scattering events per unit length. Moreover, the bulk electrochemical splitting per lattice site is approximated as

$$\Delta\mu_b=J_b\left(\frac{2Me^2\mathcal{T}_b}{hA}\right)^{-1} \tag{9}$$

and can be obtained from the bulk current density J_b. The experimental Ag(111) films conduct in the weak scattering limit, where the local transmission per mode approaches unity such that $\mathcal{T}_b=0.995$ and $\Delta\mu_b\approx J_bhA/2Me^2$. This can be shown by returning to Eq. (8) and plugging in the Ag(111) (Ref. 5) values $\sigma=(2.2\times10^{-6}\ \Omega\ \mathrm{cm})^{-1}$, $M/A=11.3\ \mathrm{nm}^{-2}$, and $\nu_b=1/2.89$ Å. The bulk Ag(111) value M/A is taken from Table I (in the absence of back scattering $M/A=\mathcal{T}/A$).

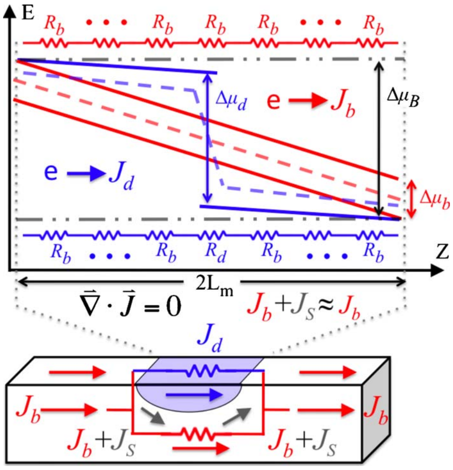

FIG. 5. (Color online) Bulk diffuse phonon scattering is shown in red where the electrostatic potential drop follows the electrochemical potential drop. The length scale $2L_m$ is much greater than that shown in Fig. 1. Local-defect scattering is shown in blue, where due to the enhanced scattering strength of the defect a resistivity dipole develops (see Sec II). The dashed line color coded to each scenario displays the average quasi-Fermi level (Ref. 15) between left bound and right bound scattering electrons. The incident bulk current scattered by the defect is denoted as J_s. The defect ballistic scattering region with current density J_d and surrounding bulk scattering medium with current density $J_s+J_b\approx J_b$ can be approximated as two resistances conducting in parallel (Ref. 46).

An atomic-sized defect introduced into the Ag(111) bulk scattering medium can be treated as an additional series mode resistance[46] $R_d=(1-\mathcal{T}_d)h/\mathcal{T}_d2e^2$ with transmission $\mathcal{T}_d$ (see Fig. 5). The applied bias drops in series across the defect and bulk scattering regions. A strongly scattering $\mathcal{T}_d\to0$ or high-resistance defect perturbs the linear bulk electrochemical potential drop and forms a resistivity dipole (as shown in Fig. 5),[16] within which the electrochemical potential no longer follows electrostatic potential. The greater the resistance of the defect, the further the defect diverges from the weak scattering regime such that $\Delta\mu_d>\Delta\mu_b$ (as highlighted in blue in Fig. 5). Only a weakly scattering defect ($\mathcal{T}_d\approx1$ for all modes) will posses an electrochemical potential drop $\Delta\mu_d$ that is well approximated by the bulk electrochemical splitting such that $\Delta\mu_b\approx\Delta\mu_d$.

We can directly evaluate the low-bias mode-resolved transmission of the Ag(111) step edge and chain defects highlighted in Fig. 2 by decomposing the 12-layer scattering system into eigenchannels.[27] The mode-resolved transmission $\mathcal{T}_{d,i}(\mu_{eq},k_x)$ is plotted in Figs. 6(a) and 6(b) across 20 sampled transverse k_x vectors at the equilibrium electrochemical potential μ_{eq}. A given ith mode can be understood as a separate conducting band in the material bandstructure at the Fermi energy, where the transmission of a band is unity in the absence of scattering. Note, that the k_y vectors are quantized in the plane of the assumed slab geometry and do not contribute to the Brillouin zone perpendicular to the transport z direction (see Fig. 2).

It is evident that some modes scatter strongly $\mathcal{T}_{d,i}(\mu_{eq},k_x)\ll1$ (shown in blue)[47,48] while others scatter weakly $\mathcal{T}_{d,i}(\mu_{eq},k_x)\approx1$ (shown in green). Those modes which scatter strongly contribute to a local defect electrochemical splitting $\Delta\mu_d$ resistivity dipole[16] that is greater than

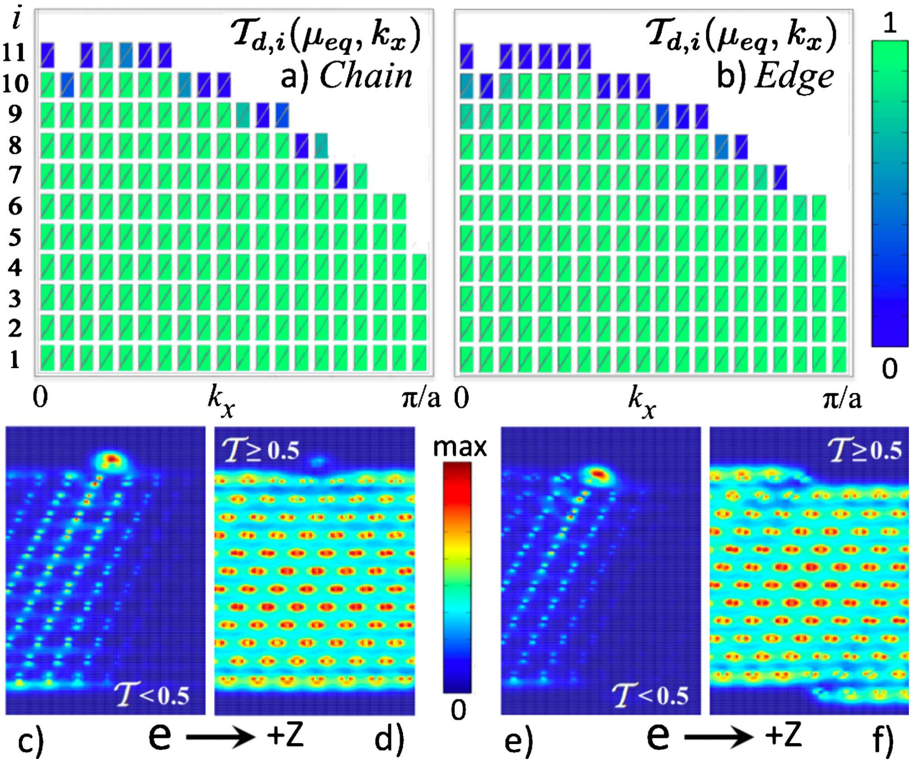

FIG. 6. (Color online) The transmission and scattering properties at μ_{eq} for 12-layer Ag(111) atomic chain and step-edge defects (Ref. 47). Figures 6(a) and 6(b) display the mode-resolved eigenchannel transmission $\mathcal{T}_{d,i}$ for each mode index i (the number of scattering modes varies across the transverse Brillouin zone). Figures 6(c) and 6(e) display the scattering charge density $\Delta\rho_L(\mu_{eq})$ for those eigenchannels with transmission $\mathcal{T}<0.5$. Figures 6(d) and 6(f) display the scattering charge density $\Delta\rho_L(\mu_{eq})$ for those eigenchannels with transmission $\mathcal{T}\geq 0.5$. All eigenchannels have a transmission of 1 for a perfectly crystalline clean Ag(111) 12-layer slab.

the average bulk electrochemical splitting $\Delta\mu_b$. Moreover, Figs. 6(c)–6(f) show change density plots $\Delta\rho_L(\mu_{eq})$ of left-scattering modes at the Fermi energy with transmission $\mathcal{T}_{d,i}<0.5$ and $\mathcal{T}_{d,i}>0.5$. Those modes which strongly scatter contribute substantially to the electron density in the vicinity of a surface defect and thereby largely determine the local-defect resistivity dipole electrochemical potential splitting (and wind force as we argue in the next section). Therefore we conclude that Ag(111) step-edge-type surface defects tend to reside in the "strong" scattering limit $\Delta\mu_d>\Delta\mu_b$ rather than in the weak scattering limit where the bulk wind force assumption $\Delta\mu_d\approx\Delta\mu_b$ applies.

2. Electrochemical potential drop across a defect

To estimate the defect electrochemical splitting $\Delta\mu_d$ and wind force F_{w_d} enhancement due to each scattering mode we return the local resistance model in Fig. 5. We treat each scattering mode independently and assume a mode specific local nonequilibrium defect electrochemical splitting of $\Delta\mu_{d,i}$. In this regard it is important to note that electrons near a scatterer are not in equilibrium. Hence, the average local electrochemical splitting $\Delta\mu_d$ only provides a count of the number of electrons near a scatterer, it does not describe the energetic distribution of electrons.[15] A nonequilibrium self-consistent model including both diffuse phonon scattering[10,39] and applied bias electrostatic boundary conditions[33] is left to future work.

Current-carrying electrons reflect ballistically off a defect and travel approximately one mean-free path L_m before losing their momentum and scattering diffusively within the phonon bath.[16] The defect current density within the ballistic scattering region $\pm L_m$ is given by $J_d=J_b-J_s$ (as shown in Fig. 5), where the incident bulk current J_b is reduced by the scattered current J_s. At the ballistic scattering region boundary $\pm L_m$ the scattered current density J_s has lost all of its backscattering momentum, therefore the boundary current density is given by the incident electron current J_b. Thus, beyond the ballistic scattering region the electrochemical potential and electrostatic potential profile follow each other linearly and are well described by Ohm's law $J_b=\mathcal{E}_b/\sigma$. Outside of the ballistic scattering region, the influence of a localized atomic scatterer on the current density and electrochemical potential drop can be largely ignored.

Within the ballistic scattering region $\pm L_m$ surrounding a defect, one can treat the diffuse onsite resistance $R_b=(1-\mathcal{T}_b)h/\mathcal{T}_b 2e^2$ as acting in series with the defect resistance of a given mode $R_{d,i}=(1-\mathcal{T}_{d,i})h/\mathcal{T}_{d,i}2e^2$ as shown in Fig. 5. Therefore the total resistance across the ballistic scattering region due to the ith mode may be approximated as $R_{B,i}=2L_m R_b \nu_b + R_{d,i}$.[49] Upon applying Ohm's law $J_b=\sigma\mathcal{E}_b$ and the relation $2L_m\mathcal{E}_b=\Delta\mu_b$ (Ref. 15) to Eqs. (8) and (9), we arrive at a bulk scattering ballistic region resistance contribution per mode of $2L_m R_b \nu_b = h/\mathcal{T}_b 2e^2 \approx h/2e^2$. Moreover, all modes may be viewed as conducting in parallel across the ballistic scattering region and subject to the electrochemical bias $\Delta\mu_B$ between left and right electrons incident from the diffusive scattering medium (see Fig. 5). Through the transmission relation $R_{B,i}=(1-\mathcal{T}_{B,i})h/\mathcal{T}_{B,i}2e^2$ we arrive at a mode specific defect current density of $I_{B,i}=I_{d,i}=2e^2\Delta\mu_B\mathcal{T}_{B,i}/h$. After some algebra the defect electrochemical splitting per mode is finally given by $\Delta\mu_{d,i}=I_{d,i}h/2e^2\mathcal{T}_{d,i}=\Delta\mu_B/(1+\mathcal{T}_{d,i})$.

An approximate estimate for $\Delta\mu_B$ can be arrived at by further considering the boundary between the bulk scattering region and ballistic scattering region. The bulk scattering region electrochemical potential (in which the defect is imbedded) and ballistic scattering region electrochemical potential are equal at the ballistic region boundary of $\pm L_m$ (see Fig. 5). The electrochemical potential drop across a bulk scattering region of length $2L_m$ is $2L_m\mathcal{E}_b=\Delta\mu_b$. Moreover, the electrochemical splitting between left bound and right bound bulk current J_b carrying states at the ballistic boundary is $\Delta\mu_b$ (highlighted in red in Fig. 5). By summing both of these contributions we arrive at an estimate of $\Delta\mu_B=2\Delta\mu_b$ for the ballistic region electrochemical bias. The electrochemical splitting per mode is therefore estimated to be

$$\Delta\mu_{d,i}=\left(\frac{2\Delta\mu_b}{1+\mathcal{T}_{d,i}}\right), \tag{10}$$

which obeys the limiting case $\Delta\mu_{d,i}\rightarrow\Delta\mu_b$ as $T_{d,i}\rightarrow 1$ (see Sec. III B).[49] Moreover, it is assumed that the current scattered by the defect I_s only slightly perturbs the bulk current density in the medium surrounding the defect such that $J_b+J_s\approx J_b$. Where any increase in the local current density will yield a proportional increase in the local voltage drop via $J=\mathcal{E}/\sigma$. This is a reasonable assumption considering the 100-nm thickness of experimental[5] Ag(111) thin films and the relatively minute size of an atomic scatterer. Even in the extremely thin simulated 12-layer slabs, the scattered defect current J_s only perturbs the bulk current density J_b by approximately 10% (see $\mathcal{T}/A$ values given in Table I). Conceptually the above approximation amounts to treating the ballistic scattering defect region and the surround bulk scattering medium as two resistances conducting in parallel subject a bias of $\Delta\mu_B=2\Delta\mu_b$ (as shown in Fig. 5).

To estimate the wind force contribution per mode (or eigenchannel) we return to Eq. (7), where the low-bias charge-density deviation is now given by

$$\Delta\rho_d\approx\sum_i\Delta\mu_{d,i}[\rho_{L,i}(\mu_{eq})-\rho_{R,i}(\mu_{eq})]/2. \tag{11}$$

The mode summation index in Eq. (11) is weighted across all sampled transverse k_x vectors (see Fig. 6) and $\Delta\mu_{d,i}$ is given by Eq. (10) (see also Fig. 5). The quantity $\rho_{L/R,i}(\mu_{eq})$ describes the local density-of-states contribution[27] of left/right scattering electrons in the ith eigenchannel.[50] Note that Eq. (11) does not invalidate Eq. (4) but rather expresses the quasi-Fermi-level splitting of each mode independently, such that $\Delta\mu_{d,i}=\mu_{L,i}-\mu_{R,i}$. The above revised low-bias charge-density deviation results in the defect wind-force F_{w_d} and effective charge $Z^*_{w_d}$ values presented in Table II. Upon taking the average value of $Z^*_{w_d}=-119$, we arrive at a local-defect wind force which agrees well with experimental estimates $Z^*_{exp}\approx-186\pm93$.

Before concluding we note that enhanced scattering also leads to an increased local-defect electrostatic potential drop via $V_d=\Delta\mu_d(1-\mathcal{T}_d)$ and in turn an increased electric field direct force $F_{\mathcal{E}_d}$ (see Sec. II). Through the linear-response relation $F_w\approx\Delta\mu_dF_w(\mu_{eq})$, the mode averaged electrochemical potential perturbation $\Delta\mu_d$ across the defect can be estimated. The average defect mode transmission may then be extracted from Eq. (10) which yields $T_d\approx0.1$. Typical self-consistent DFT single-particle Green's function transport[25–27] calculations yield a bias screening length of $L_s\approx2.5$ Å for nobel metals.[51] The local-defect electric field may then be estimated via $\mathcal{E}_d=\Delta\mu_d(1-\mathcal{T}_d)/2L_s$, which leads to a local direct force effective charge estimate through $Z^*_{\mathcal{E}_d}=\mathcal{E}_dQ_d/\mathcal{E}_b$ (note $Q_d=Z^*_{\mathcal{E}_b}$ as discussed in Sec. III B). The average local direct force effective charge is found to be $Z^*_{\mathcal{E}_d}\approx2.0$, quite a bit larger than the bulk magnitude $Z^*_{\mathcal{E}_b}\approx1.2\times10^{-2}$ as given in Table II. Nevertheless, the direct force lies well below the average wind force $Z^*_{w_d}\approx-120$ and can be ignored for the most part. However, full self-consistent nonequilibrium calculations[33] should be pursued in future efforts to properly quantify the direct force contribution.

IV. SUMMARY

Motivated by experimental reports of an enhanced electromigration force[5,18] we have analyzed the scattering properties of step edge and chain defects situated on the Ag(111) surface within the first-principles DFT single-particle Green's function Landauer transport picture.[25–27] Though most scattering modes interact weakly with a surface defect, those that scatter strongly often transmit well below unity and contribute substantially to the electron density within such a defect. We hypothesize that both of these effects lead to a nonequilibrium electrochemical potential drop across a defect, which is not well described by the bulk conduction picture. First-order estimates of the defect electrochemical splitting under bias were shown to produce a nonequilibrium wind force that agrees well with experimental observations of an enhanced electromigration force.[5] In contrast, bulk conduction wind-force estimates were found to lie below experimental error margins. To explore the applicability of the presented model to more general systems, future studies should consider the effects of phonon scattering,[10,39] self-consistency in defect screening,[10] and more complex device geometries.[18] Overall, this work underscores the need for a quantum transport nonequilibrium approach in the analysis of defect electromigration.

ACKNOWLEDGMENTS

We thank S. Datta for helpful discussions on electron transport and D. Xiao for discussions on joule heating. We gratefully acknowledge computational support and resources provided by the National Science Foundation Network for Computational Nanotechnology (Purdue). K. H. Bevan gratefully acknowledges support from NSERC of Canada (McGill). K. H. Bevan and Z. Zhang gratefully acknowledge support from the DOE under Grant No. DE-FG02-

05ER46209 and in part by the Division of Materials Sciences and Engineering, Office of Basic Energy Sciences, DOE (ORNL). Z. Zhang gratefully acknowledges support from NSF under Grant No. DMR-0906025 (UTK). E. D. Williams gratefully acknowledges support from the University of Maryland NSF-MRSEC under Grant No. DMR 05-20471. H. Guo gratefully acknowledges financial support from NSERC of Canada, FRQNT of Quebec, and CIFAR (McGill).

---

*bevankh@ornl.gov

[1] International Technology Roadmap for Semiconductors (http://www.itrs.net/Links/2007ITRS/Home2007.htm, 2007).

[2] S. M. Rossnagel and T. S. Kuan, J. Vac. Sci. Technol. B **22**, 240 (2004).

[3] E. D. Williams, O. Bondarchuk, C. G. Tao, W. Yan, W. G. Cullen, P. J. Rous, and T. Bole, New J. Phys. **9**, 387 (2007).

[4] Y. Ke, F. Zahid, V. Timoshevskii, K. Xia, D. Gall, and H. Guo, Phys. Rev. B **79**, 155406 (2009).

[5] O. Bondarchuk, W. G. Cullen, M. Degawa, E. D. Williams, T. Bole, and P. J. Rous, Phys. Rev. Lett. **99**, 206801 (2007).

[6] Q. Huang, C. M. Lilley, and R. Divan, Nanotechnology **20**, 075706 (2009).

[7] D. R. Strachan, D. E. Johnston, B. S. Guiton, S. S. Datta, P. K. Davies, D. A. Bonnell, and A. T. Charlie Johnson, Phys. Rev. Lett. **100**, 056805 (2008).

[8] M. F. G. Hedouin and P. J. Rous, Phys. Rev. B **62**, 8473 (2000).

[9] P. J. Rous, Phys. Rev. B **59**, 7719 (1999).

[10] R. S. Sorbello, Superlattices Microstruct. **23**, 711 (1998).

[11] D. N. Bly and P. J. Rous, Phys. Rev. B **53**, 13909 (1996).

[12] P. Kumar and R. S. Sorbello, Thin Solid Films **25**, 25 (1975).

[13] A. Lodder, Physica A **158**, 723 (1989).

[14] R. P. Gupta, Phys. Rev. B **25**, 5188 (1982).

[15] S. Datta, *Electronic Transport in Mesoscopic Systems* (Cambridge University Press, Cambridge, 1996).

[16] R. Landauer, Z. Phys. B **21**, 247 (1975).

[17] R. M. Feenstra and B. G. Briner, Superlattices Microstruct. **23**, 699 (1998).

[18] C. Tao, W. G. Cullen, and E. D. Williams, Science **328**, 736 (2010).

[19] N. N. Negulyaev, V. S. Stepanyuk, L. Niebergall, P. Bruno, W. Hergert, J. Repp, K.-H. Rieder, and G. Meyer, Phys. Rev. Lett. **101**, 226601 (2008).

[20] A. V. Latyshev, A. L. Aseev, A. B. Krasilnikov, and S. I. Stenin, Surf. Sci. **213**, 157 (1989).

[21] S. Stoyanov, Jpn. J. Appl. Phys. **30**, 1 (1991).

[22] J. Hoekstra, A. P. Sutton, T. N. Todorov, and A. P. Horsfield, Phys. Rev. B **62**, 8568 (2000).

[23] S. Heinze, N.-P. Wang, and J. Tersoff, Phys. Rev. Lett. **95**, 186802 (2005).

[24] R. S. Sorbello, Phys. Rev. B **31**, 798 (1985).

[25] J. Taylor, H. Guo, and J. Wang, Phys. Rev. B **63**, 245407 (2001).

[26] M. P. Anantram, M. S. Lundstrom, and D. E. Nikonov, Proc. IEEE **96**, 1511 (2008).

[27] M. Paulsson and M. Brandbyge, Phys. Rev. B **76**, 115117 (2007).

[28] M. Di Ventra and S. T. Pantelides, Phys. Rev. B **61**, 16207 (2000).

[29] D. Kandel and E. Kaxiras, Phys. Rev. Lett. **76**, 1114 (1996).

[30] J. P. Dekker and A. Lodder, J. Phys.: Condens. Matter **10**, 6687 (1998).

[31] G. C. Liang, A. W. Ghosh, M. Paulsson, and S. Datta, Phys. Rev. B **69**, 115302 (2004).

[32] A. Lodder, Defect Diffus. Forum **261-262**, 77 (2007).

[33] D. Waldron, L. Liu, and H. Guo, Nanotechnology **18**, 424026 (2007).

[34] K. H. Bevan, T. Low, and H. Guo, J. Appl. Phys. **105**, 093709 (2009).

[35] J. M. Soler, E. Artacho, J. D. Gale, A. García, J. Junquera, P. Ordejón, and D. Sánchez-Portal, J. Phys.: Condens. Matter **14**, 2745 (2002).

[36] *CRC Handbook of Chemistry and Physics* (CRC Press, New York, 2009).

[37] N. Troullier and J. L. Martins, Phys. Rev. B **43**, 1993 (1991).

[38] S. García-Gil, A. García, N. Lorente, and P. Ordejón, Phys. Rev. B **79**, 075441 (2009).

[39] S. Datta, in *The Oxford Handbook on Nanoscience and Nanotechnology: Frontiers and Advances*, edited by A. V. Narlikar and Y. Y. Fu (Oxford University Press, Oxford, 2009).

[40] S. Ramo, J. R. Whinnery, and T. Van Duzer, *Fields and Waves In Communication Electronics*, 3rd ed. (Wiley, New York, 1994).

[41] S.-J. Tang, Y. R. Lee, S. L. Chang, T. Miller, and T. C. Chiang, Phys. Rev. Lett. **96**, 216803 (2006).

[42] M. Di Ventra, *Electron Transport in Nanoscale Systems* (Cambridge University Press, Cambridge, 2008).

[43] Inelastic effects are unlikely to contribute to low-bias electromigration (Ref. 42) and considerable care was taken in experimental measurements (Refs. 5 and 18) to minimize joule heating.

[44] D. B. Tanner and D. C. Larson, Phys. Rev. **166**, 652 (1968).

[45] R. Venugopal, M. Paulsson, S. Goasguen, S. Datta, and M. S. Lundstrom, J. Appl. Phys. **93**, 5613 (2003).

[46] I. Matsuda, M. Ueno, T. Hirahara, R. Hobara, H. Morikawa, C. Liu, and S. Hasegawa, Phys. Rev. Lett. **93**, 236801 (2004).

[47] Note that surface states only extend along approximately one-tenth of the transverse k_x Brillouin zone (Ref. 48).

[48] L. Bürgi, L. Petersen, H. Brune, and K. Kern, Surf. Sci. **447**, L157 (2000).

[49] Regarding electrons scattering at transverse k_x wave vectors, note that one could consider also average over the ballistic distance traveled by all conducting Fermi sphere electrons in the z direction which is $2L_m/\pi$. The electrochemical splitting in the Fermi surface, when averaged over the mean-free path in the transport direction, is then $4L_m/\pi\mathcal{E}_b=\Delta\mu_b$. All of the resistance ratios and the electrochemical potential drop within the ballistic region work out again to produce Eq. (10).

[50] M. Büttiker, Y. Imry, R. Landauer, and S. Pinhas, Phys. Rev. B **31**, 6207 (1985).

[51] M. Brandbyge, J.-L. Mozos, P. Ordejón, J. Taylor, and K. Stokbro, Phys. Rev. B **65**, 165401 (2002).